Journal of Machine Engineering, 2024, Vol. 24, No. 2, 5-17
ISSN 1895-7595 (Print) ISSN 2391-8071 (Online)

Received*: 10 May 2024* / Accepted: *03 June 2024* / Published online: *07 June 2024*

fracture mechanics,
tool wear modelling,
microstructure of tool material

Hossein GOHARI[1],
Bin SHI[2],
M. Helmi ATTIA[3*],
Rachid M'SAOUBI[4]

FRACTURE MECHANICS-BASED MODELLING OF TOOL WEAR IN MACHINING TI6AL4V CONSIDERING THE MICROSTRUCTURE OF CEMENTED CARBIDE TOOLS

This study introduces a new wear model that can predict tool life in the milling process of Ti6Al4V using a cemented carbide tool. The model uses a finite element (FE) simulation to predict crack growth in the tool material microstructure. The FE model evaluates the crack propagation rate based on the real microstructure of the tool material, which is captured from microscopic images. To determine the normal and tangential forces operating on the flank face, an experimental procedure was developed based on three different flank wear widths. The FE model utilizes the elastic and fracture properties of tungsten carbide, and the elastic-plastic and fracture characteristics of cobalt binder to determine crack growth under the applied cutting forces. The crack propagation information combined with cutting conditions and the initial wear level are used to estimate the tool wear state. The developed model can predict tool life under different cutting conditions, tool geometries, and microstructure properties. Analysis of results showed that the error for the straight cuts was less than 6%, while for the complex cuts, it reached up to 20%. The accuracy of the model can be improved by extending the calibration test to higher levels of flank wear.

1. INTRODUCTION

One of the major challenges in machining research is tool life prediction. The challenge arises from the complexity in estimating the cutting state, and the uncertainties involved in modelling the behaviour of the tool material at various cutting conditions. Incorporating a microstructure model of the tool material in numerical simulations can significantly improve prediction accuracy. Cemented carbide, a multi-phase material extensively employed in the industry, exhibits a high degree of sensitivity to internal microstructural features such as grain

[1] Mechanical Engineering, McGill University, Canada
[2] Aerospace Manufacturing Technologies Centre (AMTC), National Research Council Canada (NRC), Canada
[3] Mechanical Engineering Dept., McGill University /, Aerospace Manufacturing Technology Centre, National Research Council Canada, Canada
[4] R&D Material and Technology Development, Seco Tools AB, Sweden
[*] E-mail: helmi.attia@mcgill.ca
https://doi.org/10.36897/jme/189588

size and distribution, morphology, and constituent phases [1]. Cemented carbide is a valuable hard material that possess exceptional combination of hardness and toughness, making it a major choice for various machining operations. It consists of two primary phases: tungsten carbide (WC) and cobalt (Co), each possesses distinct mechanical properties. The WC phase, considered as the brittle constituent, contributes to the material's hardness and wear resistance. The Co phase, referred to as the binder, is ductile and responsible for the alloy's toughness. It behaves as an elasto-plastic material [2].

In modelling, a representative volume element (RVE) is beneficial in representing the microstructural features of composite materials [3]. It serves as the minimum sample size for determining effective material parameters and provides a utility to investigate the impact of internal defects, such as micro-voids, on the stress-strain behaviour. RVEs for polycrystalline microstructures can be constructed using electron backscatter diffraction (EBSD) imaging or via scanning electron microscopy (SEM) [4]. Several software packages have been developed to capture the internal geometry of the microstructure based on SEM images such as OOF (object-oriented finite element) [5], OOF3D [6], and MIPAR™ [7]. The construction of multi-phase material microstructures can be synthetically generated using various statistical and numerical methods such as Voronoi tessellations [2], DREAM.3D [8], Monte Carlo [9], and CCBuilder [1, 2]. These methods enable the reconstruction of 2D, and 3D microstructures based on statistical descriptors that can be evaluated from 2D images. Information such as grain size, grain shape, and neighbour distributions are required to replicate the microstructure in 3D as shown in Fig. 1 [10].

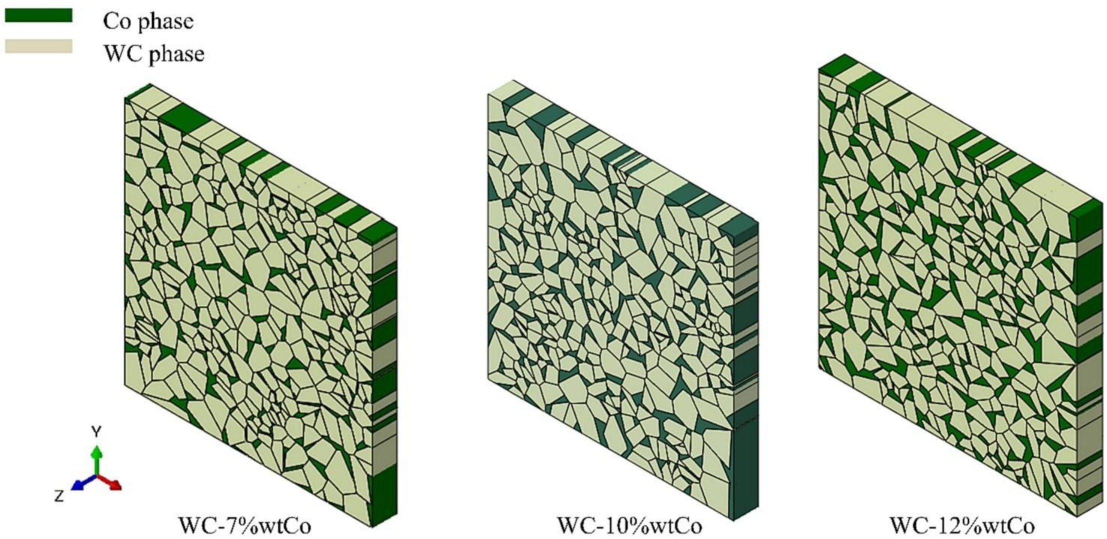

Fig. 1. Synthetic microstructures generated for WC/Co based on Voronoi algorithm [10]

2. CRACK PROPAGATION IN TOOL MATERIAL

Tool wear on the flank and rake surfaces occur due to the thermo-mechanical interaction of the cutting tool with newly created surfaces of the workpiece. The main mechanisms of tool wear are abrasion, attrition, adhesion, diffusion, and oxidation. Diffusive and oxidation wear are thermally-activated wear mechanisms, while abrasion, attrition, and adhesion are mechanically-activated wear phenomena. Mechanically-activated wear can be determined through a finite element simulation of crack propagation in tool material [11, 12]. Thermally activated wear is particularly important in machining difficult-to-cut materials such as titanium alloys. Recently, Malakizadi et al. [13] proposed a new thermodynamic model that provides an accurate prediction of dissolution-diffusion-induced tool wear of carbide tools on the flank and rake surfaces. This physics-based wear model is combined with FE simulation of the machining process and Artificial Neural Network (ANN), eliminating the need for real time temperature measurement, as required by the original model of Kramer and Suh [14]. Models for predicting different tool wear mechanisms can be found in recent review papers [15–21], which discuss advanced techniques such as artificial neural network, deep learning and machine learning systems, Gaussian process regression (GPR) models, and adaptive neuro fuzzy inference system (ANFIS).

Fig. 2 depicts a schematic for a comprehensive approach for tool life prediction. The mechanically activated wear, which is the focus of this investigation, includes FE analysis of crack propagation in the tool material, considering its microstructural features. In this analysis, a representative unit cell is constructed to model the material behaviour within the FEA. A crack cell is embedded within the unit cell to determine the fracture properties, such as crack tip displacement (CTD).

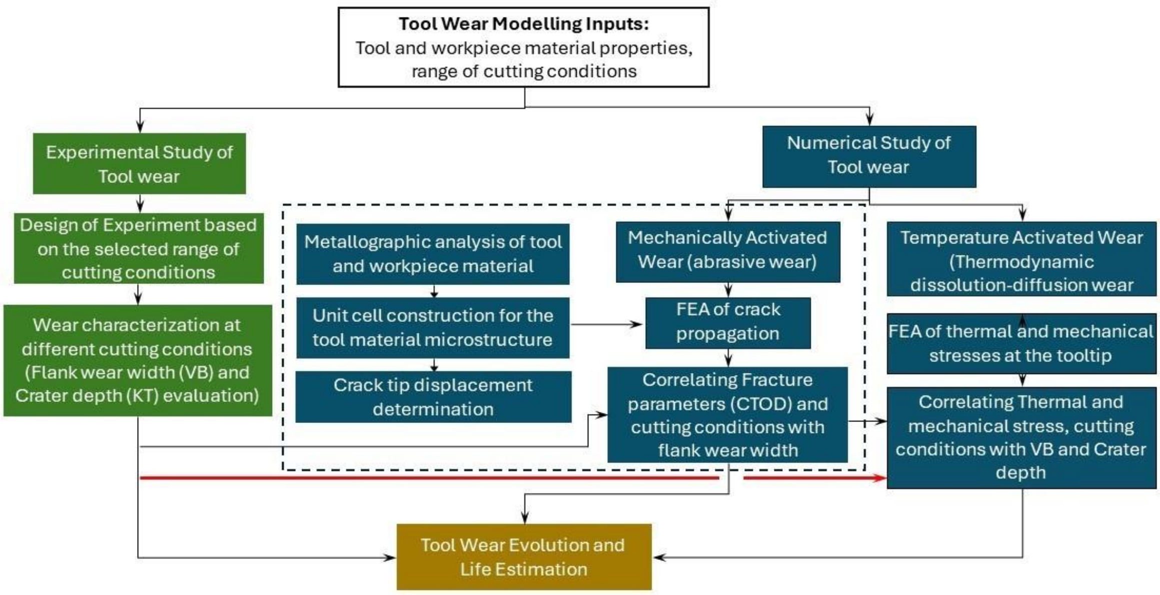

Fig. 2. Tool life estimation methodology

It has been observed that cracks in WC/Co alloys extend through both the brittle and ductile phases. The initial fracture occurs within the brittle tungsten carbide (WC) grains, creating a zone with multiple microcracks at the crack tip. Subsequently, the crack propagates through the cobalt (Co) binder phase in a ductile manner [22]. However, for materials such as WC/Co carbides with an elastic-plastic behaviour and anisotropic microstructure, the material's resistance to crack growth is not constant and varies with crack length. Two primary methodologies are employed to simulate crack propagation in cemented carbides: (a) the crack tip displacement (CTD) analysis for small crack increments and (b) the continuum damage mechanics (CDM) approach for larger-scale simulations. The CTD method is primarily suited for low-cycle loading scenarios [11]. The relationship between crack growth rate (da/dN) and the range of stress intensity factor (ΔK) is commonly presented by the following relationship [23]:

$$\frac{da}{dN} = C(\Delta K)^n \tag{1}$$

where a represents the crack length, N is the number of cycles, and C and n are material constants. The applicability of linear elastic-plastic fracture mechanics (LEFM) for predicting crack growth is limited to the initial stages, particularly for cracks with dimensions on the order of grain size [11]. Crack propagation rate of small cracks is influenced by variations in the crystallographic grain orientation and the proximity of other cracks [24]. The dominant mechanism for small crack propagation is shear decohesion within slip bands located near the crack tip, causing the crack to advance in the direction of maximum shear stress. An empirical model for the crack propagation rate under mixed-mode loading conditions of normal and shear stresses is presented by Equation 2 [11]:

$$\frac{da}{dN} = A(\Delta CTD)^m \tag{2}$$

where $\Delta CTD=|\Delta\delta_P+\Delta\delta_S|$ represents the total crack tip displacement quantified from the primary and secondary slip components at the crack tip. The parameters A and m are empirical constants. The quantity ΔCTD can be evaluated from a FEA by estimating the total crack tip displacement after applying the loads [11, 22]:

$$\Delta CTD = \sqrt{\Delta CTSD^2 + \Delta CTOD^2} \tag{3}$$

where $\Delta CTSD$ and $\Delta CTOD$ refer to the relative displacement of two nodes located at the upper and lower surfaces of the crack in the tangential and normal directions to the crack plane, respectively. The location of the nodes on the upper and lower surfaces of the crack are schematically shown in Fig. 4.

3. TOOL WEAR MODEL DEVELOPMENT

Mechanically activated abrasion and attrition flank wear are caused by the gradual detachment of tungsten carbide (WC) grains from the flank face. This suggests a correlation between the rate of crack propagation in the tool microstructure and the rate of tool flank wear. Fig. 3 illustrates that the flank surface can be conceptualized as a tessellated volume filled with cubic WC grains held together with Co layers [25]. Therefore, the development of a numerical model to evaluate crack propagation rate in cobalt binder could lead to establishing an analytical model to evaluate tool wear. To improve the accuracy of the simulation of crack propagation in the tool material microstructure, the unit cell should be constructed from the real microstructure images and then embedded into the homogeneous regions to provide accurate boundary conditions, as shown in Fig. 4.

Three crack lengths have been used to evaluate the crack propagation rate in the tool microstructure in the vertical and horizontal directions: 145, 345, and 545 nm. A fixed value of the crack opening of δ=50 nm was selected, based on SEM image analysis of a crack propagated in the cemented carbide cutting tool [11].

The FE model shown in Fig. 4 consists of two regions: the homogeneous region and the microstructure cell. The former is assumed to have linear elastic behavior. The microstructure cell is discretized into two distinct phases: tungsten carbide (WC) and cobalt (Co). The WC phase is modeled as elastic, with the inclusion of a critical failure stress.

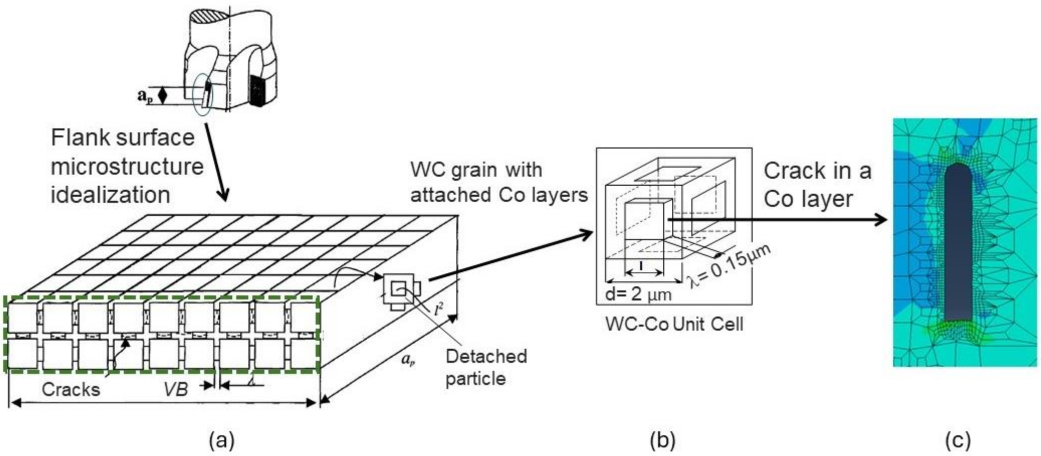

Fig. 3. Schematic representation of tool wear process on flank face: a) flank face representation [25]; b) WC grain with attached Co layers; c) meshed microstructure in ABAQUS software with an embedded crack

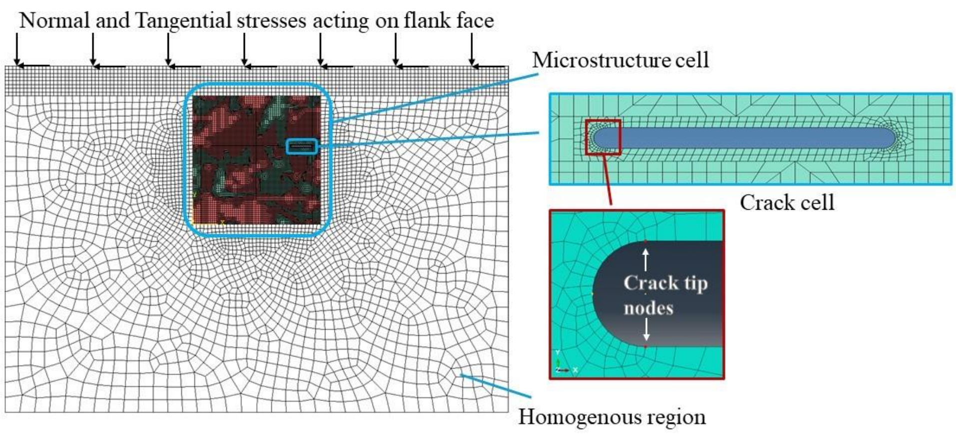

Fig. 4. Developed FE model to determine the crack propagation rate in the tool microstructure

Cobalt phase is considered to undergo both elastic and plastic deformations and fails under a critical stress. Table 1 shows the material properties reported in the open literature for each phase of WC/Co material and the homogeneous region [1, 7, 26–32]. The loading conditions are determined based on an experimental procedure to determine the normal and tangential stresses acting on the flank wear at different levels of flank wear widths. After applying the stresses, the relative displacement ΔCTD, which is empirically linked to the crack propagation rate, is calculated. The rate of detachment of a debris, and consequently wear rate, is linked to the critical length of crack in the Co binder.

Table 1. Material properties reported for WC/Co

Material	*WC* %wt	*Co* %wt	Elastic modulus *E* (GPa),	Poisson's ratio ν	Yield stress σ_y (MPa)	Hardening modulus c (GPa)	Critical failure stress σ_{IC} (MPa)
WC	100	0	700 [19], 707 [1], 697 [20], 703 [21], 715-730 [22]	0.23 [19], 0.194 [21], 0.197 [20]	-	-	4000 [19]
Co	100	0	227 [23], 223 [24], 211 [25]	0.3 [23], 0.31 [25]	683 [23]	52 [23]	1200 [7]
SECO Grade WC-12%Co	88	12	566	0.23			

As presented in [11], the length of crack to detach one debris can be assumed to be equal to twice the binder layer length (l). The volume loss ratio that belongs to a specific grain at the flank surface, $\dot{W}_1$, can be defined as:

$$\dot{W}_1 = P\frac{V_1}{S_1} \tag{4}$$

where V_1 is the volume of one WC grain, S_1 is the area of material to cut, which depends on the length of the cut L and the radial depth of cut a_e ($S_1 = L \times a_e$), and P is the probability of the crack's nucleation, which can be determined through experimental calibration. The volume of a single debris can be determined as follows [33]:

$$V_1 = d^3 + (1-G)3l^2\lambda \tag{5}$$

where *d* is the linear intercept size of carbide grains, *G* is the contiguity of the carbide grains, and λ is the mean free path in the binder or the binder layer thickness of the binder layer. This information can be determined from the metallographic analysis of the microstructure images, which are reported in Table 2. The determination of the four parameters that characterize the microstructure, namely, *d, G,* λ, and the volume fraction of binder denoted *f* is based on the linear intercept method described in [34]. The analysis was repeated six times to validate the accuracy of the parameters. The microstructure properties of two commercial tool materials (shown in Fig. 5) were compared: THM (Widia XDHT-090308-AL) was evaluated in [33], and SECO Grade WC-12%Co (indexable insert tool geometry SNHQ120302TR4-M07) was determined from the microstructure presented in [34].

Table 2. Microstructure properties of two commercial WC/Co tool material

Grade	Linear Intercept Size of Carbide Grains d, μm	Contiguity of Carbide Grains G	Binder Layer Thickness λ, μm	Volume Fraction of Binder f	Binder Layer Length l, μm
THM [26]	0.986	0.52	0.246	0.101	0.775
Seco Grade WC-12%Co	0.63	0.45	0.36	0.237	0.51

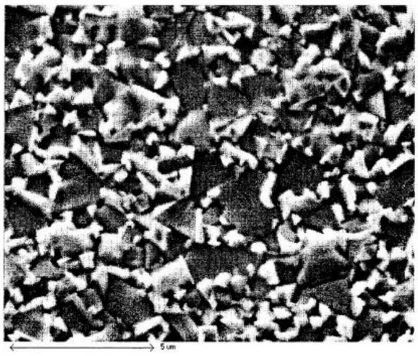

a)

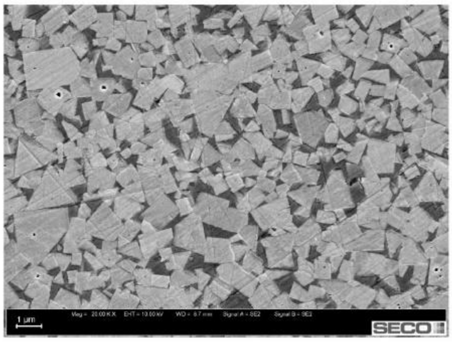

b)

Fig. 5. Microstructure images of the studied materials: a) THM [33], and b) SECO Grade WC-12%Co [34]

As explained above in discussing Equation 4, the wear rate is a function of the volume of one debris and the area of cut to detach one grain. The number of cycles q at which one debris is detached is, therefore, related to the crack propagation rate, which is a function of crack tip displacement (ΔCTD), and the critical crack length:

$$q = S_1 x \tag{6}$$

where x is the calibration factor that can be determined experimentally, and S_1 is defined as:

$$S_1 = \frac{2l}{A\, x\, (\Delta CDT)^m} \tag{7}$$

The wear rate $\dot{W}$ can now be defined as the total volume lost from the tool (V) over the area of machining S:

$$\dot{W} = \frac{V}{S} = P\frac{V_1}{S_1}N_{wc}\,, \quad S = L_t \times a_e \tag{8}$$

where L_t is the total length of the cut, a_e is the depth of cut, N_{wc} is the number of engaged WC grains in the cut which can be determined based on the area of flank wear land over the surface area of one side of the grain:

$$N_{wc} = \frac{a_p\, VB_{Bmax0}}{(d+\lambda)^2} \tag{9}$$

Where a_p is the axial depth of cut, and VB_{Bmax0} is the initial flank wear width. As explained earlier, the parameter P in Equation 4 is the crack's nucleation probability, which has a direct relationship with the surface area of cobalt binder around WC grain. Therefore, the total volume of material removed from the tool flank surface can be evaluated as follows:

$$V = a_e\, L_t\, a_p\, VB_{Bmax0}\, \frac{(1-G)\lambda(d^3 + (1-G)3l^2\lambda)}{(d+\lambda)^2}(kAx)(\Delta CDT)^m \tag{10}$$

The first three parameters are the cutting conditions (a_e, L_t, a_p), and the fraction term represents the tool microstructure constant (MSC). Finally, the current status of tool wear VB_{Bmax} can be geometrically correlated with the volumetric wear loss using the following equation [35]:

$$VB_{Bmax} = \sqrt{\frac{V}{\alpha_p(\cos\beta - \sin\beta\tan\alpha)\sin\beta}} \tag{11}$$

where α and β are the rake and clearance angles, respectively.

4. TOOL WEAR MODEL CALIBRATION AND VALIDATION

In order to determine the coefficients in the analytical flank wear model, it is necessary to conduct tests to identify the normal and tangential stress acting on the flank surface. The calibration and validation tests were conducted on a five-axis DMU 100P duoBlock machining center. Milling operation tests were carried out using a 63 mm tool with a five-flute cutter and SECO insert XOMX160508R-M09 which has SECO- Grade WC-12%Co cemented carbide substrate. Three levels of flank wear state (VB_{Bmax0}= 0, 0.1, and 0.2 mm), two levels of cutting speeds (39.6 m/min and 49.5 m/min) and feed per tooth (0.08 mm/z and 0.1 mm/z), and constant radial and axial depth of cuts (44.1 mm and 1.5 mm, respectively) were selected to evaluate the normal and tangential stresses. The cutting forces were measured using a three-component dynamometer, the KISTLER 9255B, and the 5070A KISTLER charge amplifier. The measured forces were decomposed to determine the tangential and normal stresses acting on the flank face following the procedure given in [25]. The microscope used for tool wear measurement was Zeiss Smartzoom 5 with an absolute accuracy of ±10 μm. These stresses were evaluated by subtracting the radial and tangential forces acting on the tooltip when VB_{Bmax0}=0 and then used in FE simulations to assess the crack tip displacements. Table 3 shows the test conditions for the calibration of the model and the values of the total crack tip displacement Δ*CTD* predicted by the FE analysis.

A fitting procedure was used to determine the coefficients of the wear volume model (Equation 10): (*k A x*) = 0.00091 and *m* = 3.64. The predicted volumetric wear loss and the corresponding flank wear VB_{Bmax} are given in Table 4. The table shows that VB_{Bmax} prediction error is ≤ 18%.

Table 3. Cutting conditions of the calibration tests and the FE predictions of crack tip displacements

Test #	Cutting length (mm)	Cutting speed (m/min)	Axial depth of cut a_p (mm)	Radial depth of cut a_e (mm)	feed per tooth (mm/z)	VB_{Bmaxo} (µm)	ΔCTD (nm) FEA
1	70	39.6	1.5	44.1	0.08	105	3.8
2	70	39.6	1.5	44.1	0.1	118	3.8
3	70	49.5	1.5	44.1	0.08	131	4.1
4	70	49.5	1.5	44.1	0.1	105	5.9
5	270	39.6	1.5	44.1	0.08	146	4.9
6	270	39.6	1.5	44.1	0.1	162	3.9
7	270	49.5	1.5	44.1	0.08	134	6.8
8	270	49.5	1.5	44.1	0.1	185	7.1

Table 4. Evaluated wear and cutting properties of the tests

Test #	Cutting length L_t (mm)	MSC	Measured VB_{Bmax0} (µm)	Measured VB_{Bmax1} (µm)	Measured ΔVB (µm)	Predicted V (µm^3)	Predicted VB_{Bmax1} (µm)	VB_{Bmax1} error (µm)	Error %
1	70	0.08172	105	118	13	12	114	3.7	-3%
2	70	0.08172	118	131	13	12	128	3.5	-3%
3	70	0.08172	131	173	42	120	141	31.6	**-18%**
4	70	0.08172	105	149	44	132	129	20.2	-14%
5	270	0.08172	146	162	16	17	178	-16.2	10%
6	270	0.08172	162	175	13	12	181	-6.4	4%
7	270	0.08172	134	185	51	178	202	-17.4	9%
8	270	0.08172	185	247	62	262	258	-11.2	5%

A sensitivity analysis has been carried out to determine the effect of the uncertainty of the values of the *WC/Co* material properties on the prediction of the total crack tip displacement ΔCTD, and consequently the flank wear model. The range of variation in the material properties is based on the reported values given in Table 1. The moduli of elasticity of the *WC* phase and the *Co* phase fall within the range of 650-750 GPa and 200-250 GPa, respectively. For the homogenous region, the material properties determined by the tool manufacturer (SECO) were selected. The loading condition of Test #4, and for a crack size of 345 nm were selected for this assessment. The results of the sensitivity analysis are given in Table 5 and showed that this source of uncertainty resulted in a variation of only ± 4% around an average value of ΔCTD = 3.88 nm.

Table 5. Sensitivity analysis: Variation in inputs and the evaluated crack propagation factor

Case #	Elastic modulus of *WC*, *E* (GPa)	Elastic modulus of *Co E* (GPa),	ΔCTD (nm)	Error from average value of ΔCTD
Case 1	700	227	3.84	-1%
Case 2 (*WC* high, *Co* high)	750	250	3.89	1%
Case 3 (*WC* low, *Co* low)	650	200	3.71	-4%
Case 4 (*WC* high, *Co* low)	750	200	4.03	4%
Case 5 (*WC* low, *Co* high)	650	250	3.93	2%

To validate the wear model, 11 additional tests were conducted to compare the predicted and measured flank wear, VB_{Bmax1}. Table 6 shows the cutting conditions (cutting length Lt, cutting speed v, axial depth of cut a_p, radial depth of cut a_e, and feed/tooth f_z) for eight linear cuts (L1 to L8), and three complex cuts (C1 to C3) that involve variable radial depth of cut along the tool path. The initial value of VB_{Bmax0} for test # L1 was 106 μm.

Table 6. Wear validation test conditions

Test #	L_t (mm)	v (m/min)	Axial depth of cut a_p (mm)	Radial depth of cut a_e (mm)	Feed per tooth f_z (mm/z)
L1	70	39.6	1.5	44.1	0.08
L2	70	39.6	1.5	44.1	0.10
L3	70	49.5	1.5	44.1	0.08
L4	70	49.5	1.5	44.1	0.10
L5	70	39.6	1.5	44.1	0.08
L6	70	39.6	1.5	44.1	0.10
L7	70	49.5	1.5	44.1	0.08
L8	70	49.5	1.5	44.1	0.10
C1	1092	43.5	2.5	63	0.095
C2	1092	43.5	2.5	63	0.095
C3	1092	43.5	2.5	63	0.095

For conservative assessment of the effect of uncertainty of the values of the materials' properties and to account for other sources of uncertainties, a variation of ± 8% in the estimated ΔCTD was introduced. Using Equations 10 and 11, the predicted and measured flank wear (VB_{Bmax1}) are summarized in Table 7. It can be seen that the prediction error for the linear cuts was ≤ 4%, while for the complex cuts, it was ≤ 16%. It should be noted that the model calibration was carried out for flank wear VB_{Bmax} < 200 μm, while in the third pass (C3), the flank wear reached 220 μm. The accuracy of the model can be increased by extending the calibration test to higher levels of flank wear. When the sources of uncertainties are considered (ΔCTD ±8%), the prediction error increases from 4% and 16% to 6% and 20%, for linear and complex cuts, respectively.

Table 7. Effect of variation in material properties on crack propagation

Test #	Length (mm)	Measured VB_{Bmax0} (μm)	Measured VB_{Bmax1} (μm)	Predicted VB_{Bmax1} (μm)	Prediction error (based on average ΔCTD	Prediction error (based on average ΔCTD -8%)	Prediction error (based on average ΔCTD +8%)
L1	70	101	106	107	1%	0%	2%
L2	70	106	114	112	-2%	-3%	-1%
L3	70	114	128	124	-3%	-4%	-2%
L4	70	128	146	143	-2%	-3%	0%
L5	70	185	205	202	-1%	-3%	0%
L6	70	205	219	222	1%	0%	2%
L7	70	219	250	261	**4%**	2%	**6%**
L8	70	250	297	306	3%	0%	5%
C1	1092	120	133	139	4%	15%	**20%**
C2	1092	133	159	156	-2%	10%	17%
C3	1092	159	220	190	**-16%**	0%	8%

Figures 6(a) and 6(b) show the evolution of the tool flank wear for the linear and complex validation tests, respectively. In these figures, the initial state of flank wear is represented by a dashed line. The solid lines correspond to wear measurements and the wear model predictions. Fig. 7 shows images of the worn flank face of the tool at the beginning and end of tests L8 and C3. These images show that the main wear mechanism during the cutting tests was mechanically activated.

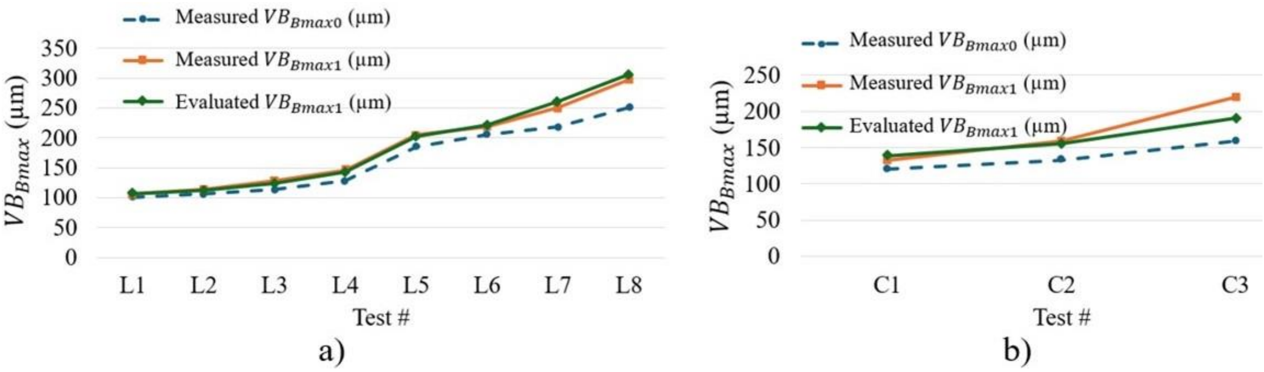

Fig. 6. Validation results; tool wear measurements: a) Linear cuts; b) Complex cuts

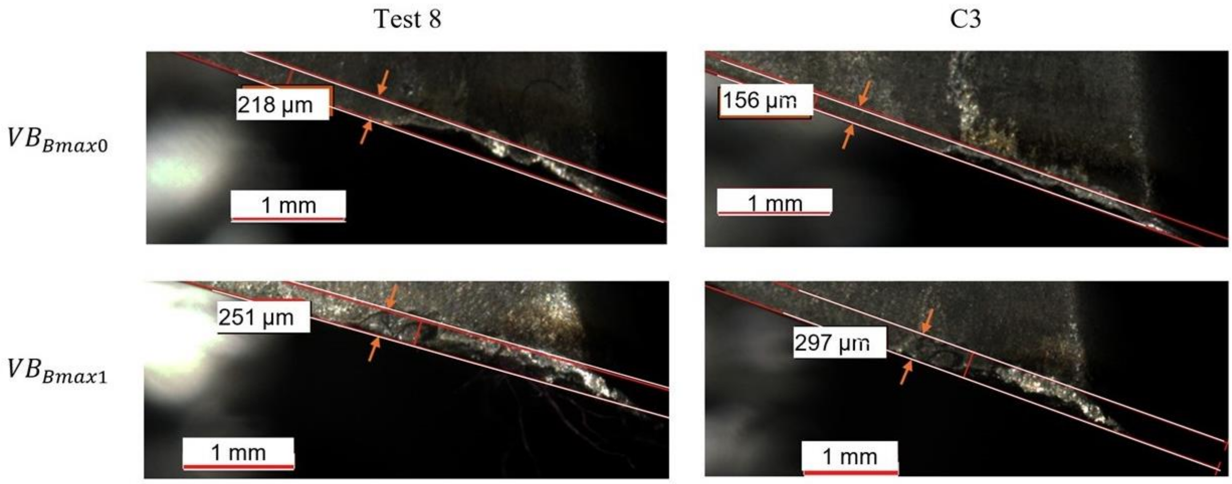

Fig. 7. Validation results; microscope images of the tool flank face

4. CONCLUSION

In this study, a fracture mechanics-based wear model was introduced to predict mechanically activated wear of cemented carbide tools in milling operations. The model incorporates the results of FE simulation of the crack propagation in the tool material, considering its real microstructure features in order to estimate the detachment rate of WC grains. The elastic and fracture properties of tungsten carbide, as well as the elasto-plastic and fracture properties of the cobalt binder were used to construct the crack propagation model.

A sensitivity analysis was conducted to assess the effect of the uncertainty of the values of the tool material properties on the estimated crack propagation rate in the cobalt binding. Following the experimental model calibration, validation milling tests were carried using carbide tools to machine Ti6Al4V alloy. The results showed that the maximum error in tool wear prediction for complex cuts is ≤ 20% when the material properties' uncertainty is considered. For future work, it is recommended to integrate the fracture mechanics model developed in this investigation with a thermodynamic model that accounts for thermally activated dissolution-diffusion tool wear.

REFERENCES

[1] GARCÍA J., et al., 2019, *Cemented Carbide Microstructures: A Review,* International Journal of Refractory Metals and Hard Materials, 80, 40–68.

[2] TKALICH D., et al., 2017, *Multiscale Modeling of Cemented Tungsten Carbide in Hard Rock Drilling,.* International Journal of Solids and Structures, 128, 282–295.

[3] KEMPESIS D., et al., 2022, *Micromechanical Analysis of High Fibre Volume Fraction Polymeric Laminates Using Micrograph-Based Representative Volume Element Models,* Composites Science and Technology, 229, 109680.

[4] MINGARD K.P., et al., 2018, *Visualisation and Measurement of Hardmetal Microstructures in 3D,* International Journal of Refractory Metals and Hard Materials, 71, 285–291.

[5] LANGER S.A., FULLER E.R., CARTER W.C., 2001, *OOF: an Image-Based Finite-Element Analysis of Material Microstructures,* Computing in Science & Engineering, 3/3, 15–23.

[6] COFFMAN V.R., et al., 2012, *OOF3D: an Image-Based Finite Element Solver for Materials Science,* Mathematics and Computers in Simulation, 82/12, 2951–2961.

[7] SOSA J.M., et al., 2014, *Development and Application of MIPAR™: A Novel Software Package for Two- and Three-Dimensional Microstructural Characterization,* Integrating Materials and Manufacturing Innovation, 3/1, 123–140.

[8] ARDELJAN M., et al., 2015, *A Study of Microstructure-Driven Strain Localizations in Two-Phase Polycrystalline HCP/BCC Composites Using a Multi-Scale Model,* International Journal of Plasticity, 74, 35–57.

[9] ALLEMAN C.N., et al., 2018, *Concurrent Multiscale Modeling of Microstructural Effects on Localization Behavior in Finite Deformation Solid Mechanics,* Computational Mechanics, 61/1–2, 207–218.

[10] AGODE K.E., et al., 2024, *Modelling of the Damage Initiation at WC/WC and WC/Co Boundaries in WC-Co Tool Material at the Microstructure Scale: Application to the Tool/Chip Contact,* International Journal of Refractory Metals and Hard Materials, 119, 106508.

[11] BARDETSKY A., ATTIA H., ELBESTAWI M., 2007, *A Fracture Mechanics Approach to the Prediction of Tool Wear in Dry High-Speed Machining of Aluminum Cast Alloys – Part 1: Model Development,* Journal of Tribology, 129/1, 23–30.

[12] ÖZDEN U.A., et al., 2015, *Mesoscopical Finite Element Simulation of Fatigue Crack Propagation in WC/Co-Hardmetal,* International Journal of Refractory Metals and Hard Materials, 49, 261–267.

[13] MALAKIZADI A., SHI B., HOIER P., ATTIA H., KRAJNIK P., 2020, *Physics–Based Approach for Predicting Dissolution–Diffusion Tool Wear in Machining,* CIRP Annals-Manuf. Techn., 69/1, 4.

[14] KRAMER B.M., SUH N.P., 1980, *Tool Wear by Solution: A Quantitative Understanding,* Journal of Engineering for Industry, 102/4, 303–309.

[15] ATTIA H., et al., 2024, *Physics Based Models for Characterization of Machining Performance – A Critical Review,* CIRP Journal of Manufacturing Science and Technology, 51, 161–189.

[16] SARIKAYA M., et al., 2021, *A State-of-the-Art Review on Tool Wear and Surface Integrity Characteristics in Machining of Superalloys,* CIRP J. Manufacturing Science and Technology, 35, 624–658.

[17] AKHTAR W., et al., 2014, *Tool Wear Mechanisms in the Machining of Nickel Based Super-Alloys: a Review,* Frontiers of Mechanical Engineering, 9/2, 106–119.

[18] MELKOTE S., et al., 2022, *100th Anniversary Issue of the Manufacturing Engineering Division Papera Review of Advances in Modeling of Conventional Machining Processes: from Merchant to the Present,* Journal of Manufacturing Science and Engineering, 144/11.

[19] SOORI M., AREZOO B., 2022, *Cutting Tool Wear Prediction in Machining Operations, a Review,* Journal of New Technology and Materials.

[20] LI B., 2012, *A Review of Tool Wear Estimation Using Theoretical Analysis and Numerical Simulation Technologies,* International Journal of Refractory Metals and Hard Materials, 35, 143–151.
[21] ZHANG Y., et al., 2021, *Tool Wear Estimation and Life Prognostics in Milling: Model Extension and Generalization,* Mechanical Systems and Signal Processing, 155, 107617.
[22] MCHUGH P.E., CONNOLLY P.J., 2003, *Micromechanical Modelling of Ductile Crack Growth in the Binder Phase of WC–Co*, Computational Materials Science, 27/4, 423–436.
[23] FLEMING J.R., SUH N.P., 1977, *Mechanics of Crack Propagation in Delamination Wear,* Wear, 44/1, 39–56.
[24] TANAKA K., NAKAI Y., YAMASHITA M., 1981, *Fatigue Growth Threshold of Small Cracks,* International Journal of Fracture, 17/5, 519–533.
[25] BARDETSKY A., ATTIA H., ELBESTAWI M., 2007, *A Fracture Mechanics Approach to the Prediction of Tool Wear in Dry High Speed Machining of Aluminum Cast Alloys – Part 2: Model Calibration and Verification,* Journal of Tribology, 129/1, 31–39.
[26] SADOWSKI T., NOWICKI T., 2008, *Numerical Investigation of Local Mechanical Properties of WC/Co Composite,* Computational Materials Science, 43/1, 235–241.
[27] LIU Y., et al., 2014, *Mechanical Properties and Chemical Bonding Characteristics of WC and W2C Compounds,* Ceramics International, 40/2, 2891–2899.
[28] SUETIN D.V., SHEIN I.R., IVANOVSKII A.L., 2008, *Elastic and Electronic Properties of Hexagonal and Cubic Polymorphs of Tungsten Monocarbide WC and Mononitride WN from First-Principles Calculations.* Physica Status Solidi (b), 245/8, 1590–1597.
[29] KIM H., KIM J., KWON Y., 2005, *Mechanical Properties of Binderless Tungsten Carbide by Spark Plasma Sintering.* in *Proceedings,* The 9th Russian-Korean International Symposium on Science and Technology, KORUS 2005, IEEE.
[30] ÖZDEN U.A., BEZOLD A., BROECKMANN C., 2014, *Numerical Simulation of Fatigue Crack Propagation in WC/Co Based on a Continuum Damage Mechanics Approach,* Procedia Materials Science, 3, 1518–1523.
[31] KARIMPOOR A.A., Erb U., 2006, *Mechanical Properties f Nanocrystalline Cobalt,* Physica Status Solidi (a), 203/6, 1265–1270.
[32] POECH M.H., et al., 1993, *FE-Modelling of the Deformation Behaviour of WC-Co Alloys,* Computational Materials Science, 1/3, 213–224.
[33] BARDETSKY A., 2005, *Tribological Behavior of Cutting Tool in High-Speed Machining of Al-Si Alloys*, McMaster University.
[34] HERRERO B.C., 2022, *Experimental Study and Modelling of Heat Transfer in Milling of Titanium Alloys, M.Sc. Thesis*, in *Production and Materials Engineering*, Lund University.
[35] ETHERIDGE R. HSU T., 1969, *The Specific Wear Rate in Cutting Tools and its Application to the Assess*ment of Machinability, Annals of CIRP, 18, 107–117.